Neural-network-enhanced evolutionary algorithm applied to supported metal nanoparticles

E. L. Kolsbjerg,[1] A. A. Peterson,[2] and B. Hammer[1,*]
[1]*Interdisciplinary Nanoscience Center (iNANO), Department of Physics and Astronomy, Aarhus University, Denmark*
[2]*School of Engineering, Brown University, Providence, Rhode Island, 02912, USA*

(Received 10 November 2017; revised manuscript received 26 April 2018; published 16 May 2018)

We show that approximate structural relaxation with a neural network enables orders of magnitude faster global optimization with an evolutionary algorithm in a density functional theory framework. The increased speed facilitates reliable identification of global minimum energy structures, as exemplified by our finding of a hollow Pt_{13} nanoparticle on an MgO support. We highlight the importance of knowing the correct structure when studying the catalytic reactivity of the different particle shapes. The computational speedup further enables screening of hundreds of different pathways in the search for optimum kinetic transitions between low-energy conformers and hence pushes the limits of the insight into thermal ensembles that can be obtained from theory.

DOI: 10.1103/PhysRevB.97.195424

I. INTRODUCTION

The field of automated structure determination [1,2] and high-throughput computational studies in condensed matter physics and materials science [3] is seeing great advances in capabilities following developments in first-principles computational methods and the advancements in computing power available. The buildup of databases of structure-property relations [4,5] enables efficient prediction of promising new materials that are not yet experimentally characterized, or even synthesized [6,7]. Such computational studies rely on accurate identification of possible ground-state and metastable structures of matter across variations in stoichiometries, symmetries, and, for extended system, also lattice parameters.

The same scenario plays out in the field of heterogeneous catalysis which has a strong record of providing insight and guidance for both computational and experimental investigations [8,9]. Coordination models have proven useful in rationalizing the catalytic activity of solid surfaces with and without imperfections [10], and descriptor-based models have led to predictions of new catalytic materials [11]. As an example, the study of oxide-supported size-selected nanoparticles of reactive metals has revealed that "each atom counts"[12]. That is, the nanoparticles are showing pronounced variations in their catalytic activity with particle size and shape [13–16], and theoreticians have sought to use computational means to unravel the underlying mechanisms [17–19].

In the search for realistic atomistic models for such systems [20–23], it has become obvious that unbiased structure search algorithms such as evolutionary algorithms [24,25] (EA), basin hopping [1,26], or minima hopping [27] algorithms are required whether it is to locate realistic geometries of nanoparticles, to identify representative catalytic sites, or to create an ensemble of different configurations. As system sizes grow and become more realistic, so does the complexity of the models needed and hence more structures must be considered before a good representation of candidates can be obtained. Any measure to reduce the number of required *ab initio* calculations is hence much valued as it provides greater opportunity to explore relevant systems [28]. One way to achieve a great speedup but still be able to preserve the accuracy of first-principles calculations is to use well-trained machine-learning potentials [29] whether it is from support-vector machine methods [30], kernel methods [29,31–36], or artificial neural networks [20,22,28,37–41] (NN). With the introduction of machine-learning (ML) models that also include forces, either as derivatives of the learned energy potential [42] or by directly training the forces [34,43], it is now possible to bring a given configuration to its local minimum configuration with no prior assumption or analysis of the interaction mode as would otherwise be needed for inexpensive classical force fields. With the newly found opportunities, several successful attempts have been proposed to combine ML and global structure optimization as, e.g., a neural-network-biased genetic algorithm [44], a combination of a neural network potential and the basin-hopping method [45], the creation of hierarchical NN libraries for multicomponent systems by generating training data from EA runs [28], and particle swarm-intelligence based global optimization involving trained Gaussian approximation potentials [46]. Recently, Wu *et al.* showed that an adaptive evolutionary algorithm that reparametrizes classic interatomic potential parameters has the possibility to achieve large accelerations over purely *ab initio* evolutionary algorithm searches [47]. Similarly, Van den Bossche *et al.* have demonstrated comparable speedups for an EA by reparametrizing a tight-binding density functional model potential [48]. However, for complex or arbitrary multielement systems, the choice and reparametrization of such potentials can be cumbersome, thereby impeding and limiting the adaptive improvement of the potentials. Here, instead we suggest retraining agnostic machine-learned potentials as unbiased auxiliary energy expressions with no initiation mode assumed, which has the prospects of circumventing issues of choosing appropriate potential expressions. For this we chose an artificial neural network that eliminates relaxations at the first-principles level

*hammer@phys.au.dk

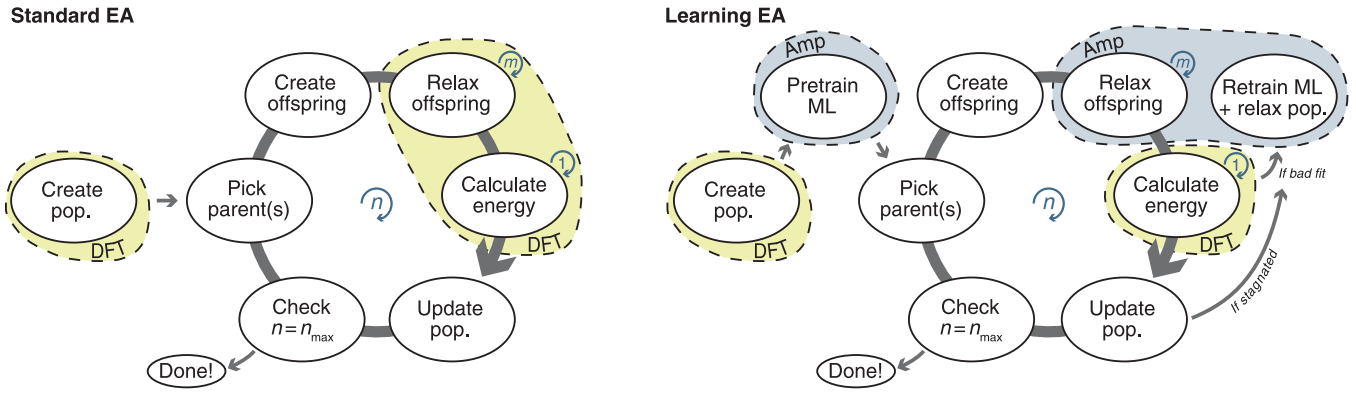

FIG. 1. Left: standard EA algorithm. Right: the proposed LEA algorithm in which new candidate structures are relaxed within the Amp model. The strategy is more conservative and hence more error tolerant than that of Ref. [47] as the model predicted energies are continuously monitored.

of theory. Following the above, we present a neural-network-enhanced evolutionary algorithm, a learning EA (LEA).

The paper is outlined as follows: We start by introducing the evolutionary algorithm, pointing out how an NN model can be trained initially and retrained on-the-fly on the steady production of new structure-energy candidates. Next, we present the details of the NN of the Behler-Parrinello [38,39] type as implemented in Amp [42] and the computational setup. We proceed by gauging the extent to which the method reduces the need for first-principles calculations. To achieve good statistics, we do this with a pseudoempirical energy expression, the effective medium theory (EMT) [49], applied to the model system of Ag_3Pt_3 nanoparticles on a Pt support. We then move to a full-scale density functional theory (DFT) investigation of MgO supported Pt particles where we apply the method showing that a combination of NN and EA enables us to unravel numerous unreported nanoparticle geometries that are considerably more stable than those previously reported. We finally investigate how the catalytic activity changes with the particle shape and effectively exploit the trained NN model to explore the transition barrier between relevant nanoparticles.

II. METHOD

The basic EA algorithm (available in the Atomic Simulation Environment (ASE) [50] and explained in details elsewhere [25]) is sketched in the left part of Fig. 1, which shows how the pool of candidates propagate towards the global minimum structure by creating a random initial population and from that picking parents to create new offsprings by pairing/mutation operations. The offsprings are relaxed to a local minimum before potentially entering the population, ideally improving the population fitness before a new loop is initiated. The expensive part of this type of global optimization algorithm is the local relaxation performed at the first-principles level. In our method, these calculations are hence circumvented by performing the relaxation in a ML model. To exclude the need for a large expensive precalculated data set for training, we chose to on-the-fly train a NN model, very much in line with NN accelerated saddle-point search proposed previously [51]. With the use of a NN model we further eliminate the need for cheaper inaccurate screening procedures like the use of classical potentials.

In this work, we chose a NN as the ML plug-in but any general ML model including force prediction is applicable and much more reliable than any classical force field [52]. To manage training, force calculation, etc., we utilize the open-source NN module of Amp, explained in detail elsewhere [42]. Amp has proven a powerful ML package with examples of its use spanning an acceleration of saddle-point searches with the nudged elastic band method [51], how dynamic Pd surfaces influence coverage-dependent oxygen interactions [53], exploring AuPd(111) slab properties [54], to predicting active CO/CO_2 sites on bimetallic nanoparticles [55]. For consistency, the construct of the NN is the same throughout this study with two hidden layers, each with five nodes to give the output atomistic energy, hence applying the atom-centered approach with the forces calculated for each atom by differentiating the energy with respect to the input parameters. The network architecture is kept simple to avoid overfitting as the variance in the data set is sparse especially for the initial training. The cosine cutoff function (radius of 7.0 Å) and the Gaussian (G2 and G4) descriptor used to describe the local structure in the region around the atoms both implemented in Amp follow the formalism suggested by Behler and Parrinello [38] with the chosen η, ζ, and γ values presented in Table I. The chosen parameters result in 40 and 72 symmetry functions per atom type for the two- and three-component systems, respectively.

The Amp structure optimization of each LEA candidate was in all cases terminated when no force exerted on any atom exceeded 0.1 eV/Å.

TABLE I. The chosen η, ζ, and γ values for the used G2 and G4 symmetry functions [39].

				G2				
η	0.01	0.05	1	4	10	20	40	80
				G4				
η	0.001	0.005						
ζ	1	4						
γ	−1	1						

The addition to the regular EA proposed in this work is illustrated in the right part of Fig. 1. First, a regular EA is initialized and the initial starting population is generated and relaxed with a total energy code of choice. We are presently resorting to two methods; the EMT [49] potential for statistical purposes and DFT for real scale systems (see details below). Before the next EA step, pairing/mutation, Amp is trained against the relaxation paths of the start population. When the training is satisfactorily converged (∼10 000 training iterations) the EA evolution proceeds but the structure relaxation is now performed at great speed with Amp instead of with the regular quantum mechanics (QM) based method. When converged to a local minimum within Amp, a single-point calculation is performed with the parent calculator and a new training point is added to the pool of training data. If there is significant discrepancy between the parent calculator and the Amp energy, $|E_{\mathrm{DFT}} - E_{\mathrm{Amp}}| > E_{\mathrm{tol}}$ (in this work chosen as 1 eV), the EA is paused and Amp is retrained based on all accumulated training data. Once the Amp energy prediction is sufficiently good, the EA proceeds as normal until it stagnates. Stagnation is here defined as $n_{\mathrm{stag}} = 40$ subsequent attempts with lower fitness than the fittest found so far. Amp is retrained (for an additional 1000 iterations) and the EA run is resumed using the optimized Amp potential. The algorithm, as any evolutionary algorithm, has no natural stopping point and is stopped once the progress is completely stagnated or after a set number of evolution steps n_{max}.

A. Effective medium theory with Ag_3Pt_3 nanoparticles

As a proof of concept, the EMT potential [49] has been employed to describe the energy of a Ag_3Pt_3 nanoparticle disposed on a Pt surface. The two-dimensional (2D) periodic model surface cell is an fcc(111) surface with the supercell spanning $4 \times 4 \times 2$ atoms with both layers held fixed. For all EMT calculations, the geometric convergence was considered achieved when no exerted force on any atom exceeded 0.025 eV/Å.

B. Density functional theory with Pt_x nanoparticles

To describe the MgO(100) supported Pt_x nanoparticle energies, we used the plane-wave method within the DFT framework of GPAW [56] with an energy cutoff of 340 and 400 eV for the parent calculator in the LEA search and final calculations, respectively. For comparability with previous studies [57,58], we used the Perdew-Burke-Ernzerhof exchange-correlation functional [59], sampling the gamma point of the Brillouin zone. The global minimum and other potential candidates were optimized in the final calculations until no forces on any atoms were above 0.025 eV/Å both with and without spin polarization. For spin-polarized calculations, the total magnetic moment was fixed at 1, 2, and 3 for each of the final structures to locate the most preferable spin configuration. Two slabs of bulk truncated MgO(100) with lattice constant 4.21 Å were used as substrate. For the LEA search, a (5×5) cell with two layers (both frozen) was utilized while a larger (7×6) cell consisting of four layers with only the bottom layer frozen was used for the post analysis. The parameters chosen for the post analysis thus conform fully with those used in Refs. [57,58].

III. RESULTS AND DISCUSSION

As NNs are interpolation methods, the performance is at best very suboptimal in regions outside the training data. The point of a global optimization algorithm such as an EA is exactly to quickly be able to search widely in parameter space in unexplored regions. This is prone to introduce structures that are not resembling those in the training data. So, why is it still possible to use a NN to optimize and evaluate the fitness of new candidates? The training data consist of a set of feature vectors centered on each atom, hence describing the local environment, and even though by the human eye a new structure might appear very different from any structure in the training set, its local feature vectors could very easily still be in the interpolated part of the training data. This is especially true as new candidates are often created by a pairing between two half-candidates (e.g., by the cut-and-splice operator). With that in mind, it is still possible, notably at the cutting plane, to create environments not possible to represent well with the current training data and hence the NN could perform unsatisfactorily. An unintended poor performance is caught as every new candidate is recalculated at the full level of accuracy, however, only as a single-point calculation with the parent calculator and added to the training data before a potential retraining is initialized.

A. Pt_3Ag_3 nanoparticles with EMT

To provide a relevant basis for a statistical analysis of the algorithm, a relative simple nanoparticle of three Pt and three Ag atoms is deposited on a Pt(111) surface. The global minimum model system is displayed in Fig. 2(a). Restarting the LEA and regular EA algorithms 100 times from scratch allows for a direct comparison between the number of candidates and parent (EMT in this case) calculations needed to locate the global minimum. In Fig. 2(b), we plot the fraction of the individual runs that have succeeded in finding the global minimum versus the improvement attempts made (or "generations") of the EA cycle (see Refs. [35,60] for a similar metric). Not surprisingly, the LEA runs are delayed in locating the global minimum before the same success rate is achieved. However, the cycle employing a neural network needs far fewer parent (*ab initio*/EMT) calculations per attempt, which is evident when we plot the same data versus the number of parent calculations [Fig. 2(c)]. Both methods need a proper starting point achieved by relaxing the initial random population 50 steps, hence, when analyzed we distinguish between the initial and the EA cycle calculations needed to propagate the search. Figure 2(b) reveals that to achieve finding the global minimum structure with 50% certainty the average number of attempts needed to make increases from ∼170 to ∼260. On the other hand, the amount of EA parent cycle calculations for the successful runs for the two strategies decreases from $\overline{n \times m} \approx 8900$ to $\overline{n} \approx 260$. The above is highlighted in Fig. 2(d). The average number of EA cycle parent calculations for the regular EA is shaded light red, where n and m introduced in Fig. 1 are the number of EA loops and parent relaxation steps, respectively. Correspondingly for the NN model, shaded light yellow, only the $\overline{n}$ EA cycle parent calculations are on average needed and if we consider the $\overline{m}$ model relaxations for basically free, which

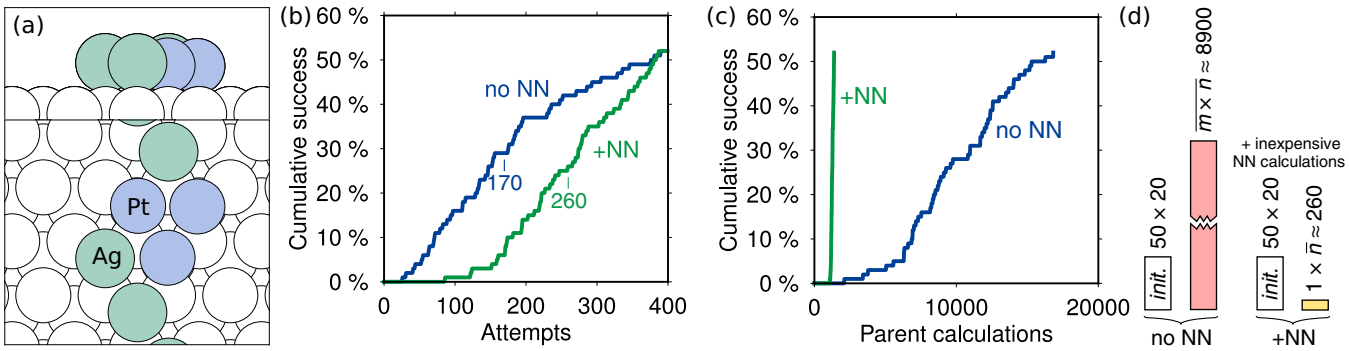

FIG. 2. (a) The atomistic model of the Pt_3Ag_3 nanoparticle supported on the Pt(111) with the Ag and Pt atoms colored green and blue, respectively, while the slab Pt atoms are white. (b), (c) The success rate of locating the global minimum as a function of the number of candidates evaluated and the number of needed parent calculations, respectively, while (d) highlights the significant reduction in the average parent calculations needed.

is a good approximation when compared to expensive DFT calculations, the difference in parent calculations is a very good representation of the amount of time on average gained when locating the global minimum. What is also evident is that a large amount of the needed parent calculations actually originate from the initial relaxation of the start population, the white bars, an amount that dominates the needed parent calculations for the LEA method. For this specific system, each LEA run requires ∼10 retraining steps, predominantly caused by stagnations.

B. Pt_x nanoparticles on MgO with DFT

Having established a robust algorithm, we apply it to a number of Pt nanoparticles on MgO which have been studied extensively for their catalytic properties both theoretically and experimentally [57,58,61–65]. A number of nanoparticle configurations of sizes 9, 10, and 13 have already been suggested from an extended search [57,58] and we employ the LEA algorithm for the exact same systems and computational setup. Running the NN accelerated EA for the three particle sizes reveals that the task of finding the right nanoparticles is indeed too complex to do by hand as several more stable configurations are located for all three sizes. For each size, we restarted the search three times and the evolution of all nine LEA runs are plotted in Fig. 3. The top 54 most stable candidates found during the LEA runs are plotted in the Supplemental Material [66], Fig. S1-3, for each particle size. The apparent global minimum is located by all three EA runs for the Pt_9 nanoparticle, and by $\frac{2}{3}$ of the runs for the Pt_{10} and Pt_{13} nanoparticles. The fact that we do not find the global minimum for every restart conforms with the findings in Fig. 2 for the Pt_3Ag_3 system, where Fig. 2(b), for instance, showed ∼50% hit rate after ∼400 attempts.

From the EA search, candidates within a ∼0.5 eV window from the top are transferred and rerelaxed in the same unit cell as used by Crampton *et al.* [57,58] Their best guess for each size is plotted in Figs. 4(c), 4(f), and 4(o). For the Pt_9 and Pt_{10} nanoparticles, the structures and the updated energies of our two best structures found are plotted in Figs. 4(a), 4(b), 4(d), and 4(e). Following Crampton *et al.*, the spin degree of freedom has been mapped and optimized for each of the structures resulting in both magnetic and nonmagnetic structures. A more extensive view of the explored structures is plotted for the Pt_{13} nanoparticles in Figs. 4(g)–4(o)which show the transition for LEA structures to the post-analyzed structures. In the top of Fig. 4(g), the density of states of uniquely found LEA candidates in the (5 × 5) cell is plotted, and just below is a zoom-in on a 0.6-eV window of the most stable candidates. Finally, at the bottom the final rerelaxed structures in the (7 × 6) cell are plotted on the same energy scale. The same analysis can be seen for the both the Pt_9 and Pt_{10} searches in the Supplemental Material [66], Figs. S4 and S5.

In general, some of the minima in the small unit cell are "false" minima and hence when transferred to the large

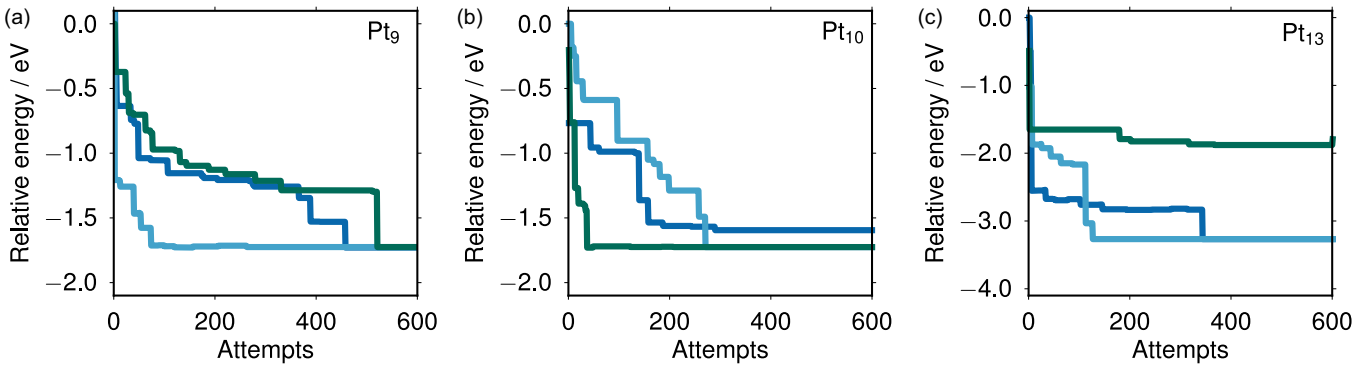

FIG. 3. The three individual LEA runs for each of the three nanoparticle sizes 9, 10, and 13 Pt atoms in (a), (b), and (c), respectively. The plots show the most stable candidate found as a function of the number of attempts.

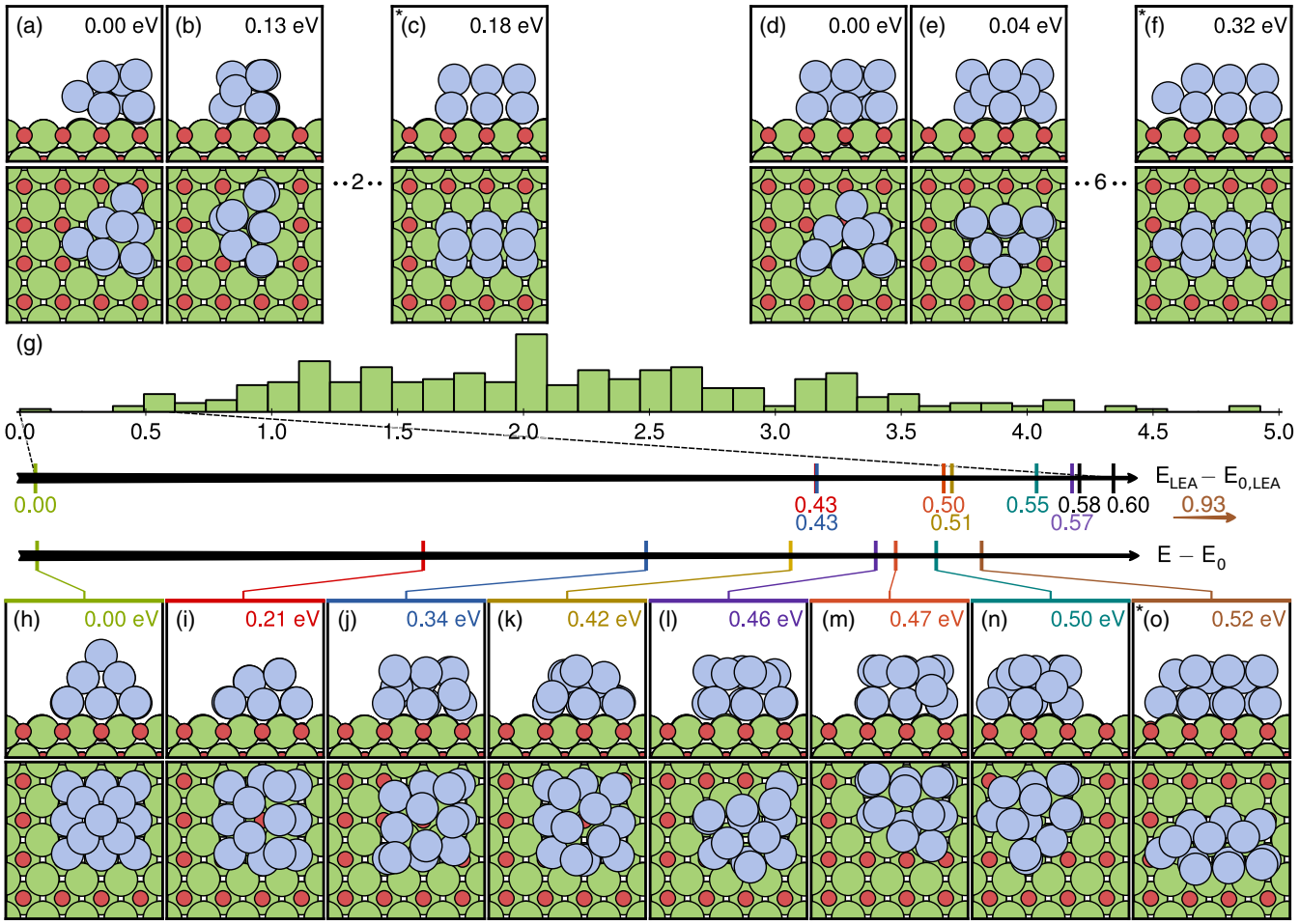

FIG. 4. Top and side views of the two most stable configurations and the previous reported (*) for the Pt_9 (a)–(c) and Pt_{10} (d)–(f). (g) From the top: the density of states for the 5-eV most stable Pt_{13} nanoparticles for all LEA runs, zoom-in on the window of the first 0.6-eV most stable particles, and the structures transferred to Crampton *et al.*'s (7 × 6) unit cell with the total magnetic moment optimized. (h)–(o) The eight best nanoparticles including Crampton *et al.*'s suggested (marked *) shown in a top view. (b), (c), (f) Have an optimized magnetic moment of 2 while (n) has a magnetic moment of 1; the remaining depicted structures are nonmagnetic. Green, red, and light blue spheres represent Mg, O, and Pt atoms, respectively.

unconstrained cell they relax into one of the other minima. The large change in energy seen for a couple of configurations is mostly due to a significant stability gain when allowed to possess a magnetic moment.

It is evident that a relevant proportion of the most stable Pt_9 structures are very asymmetric and hence even harder to guess. Out of the 10 best structures identified in our work, only three, including the previously suggested structure, have a high symmetry. The asymmetric trend is also observed for the Pt_{10} nanoparticles with the global minimum configuration showcasing four atoms twisted out of a high-symmetry configuration. A great example of a relevant peculiar deformation that a human would hardly imagine which could have relevant consequences for the catalytic property of the particle.

The situation is different for the larger Pt_{13} nanoparticles. Here, the most stable nanoparticle is very symmetric and formed like a hollow pyramid with a missing atom in the center. In hindsight, this is an obvious structure which is possible, at least in the case of Au_{13} supported on MgO(100) [67], for humans to guess but still overlooked for Pt_{13} in previous studies [57,58]. This is not a single incidence as a total of six highly symmetric structures are among the more stable geometries for the three particles sizes found in this work. In the next sections we will explore the consequences of not knowing the right particle geometry by comparing adsorption properties of the hollow pyramid [Fig. 4(h)] and the elongated structure [Fig. 4(o)] previously suggested.

C. Adsorption of CO and C_2H_4 on Pt_{13}

First, we examine the reactivity of the nanoparticles by calculating the adsorption energy, a classical catalytic descriptor. Both CO and ethylene have been adsorbed on the two different nanoparticles on any conceivable/reasonable site. All stable sites found are depicted in the top panel of Fig. 5. As the adsorption energy is site dependent, each site has been assigned a number and the corresponding adsorption potential energy can be found in Table II. For each nanoparticle, the most stable adsorption configuration has been depicted in the bottom panel of Fig. 5.

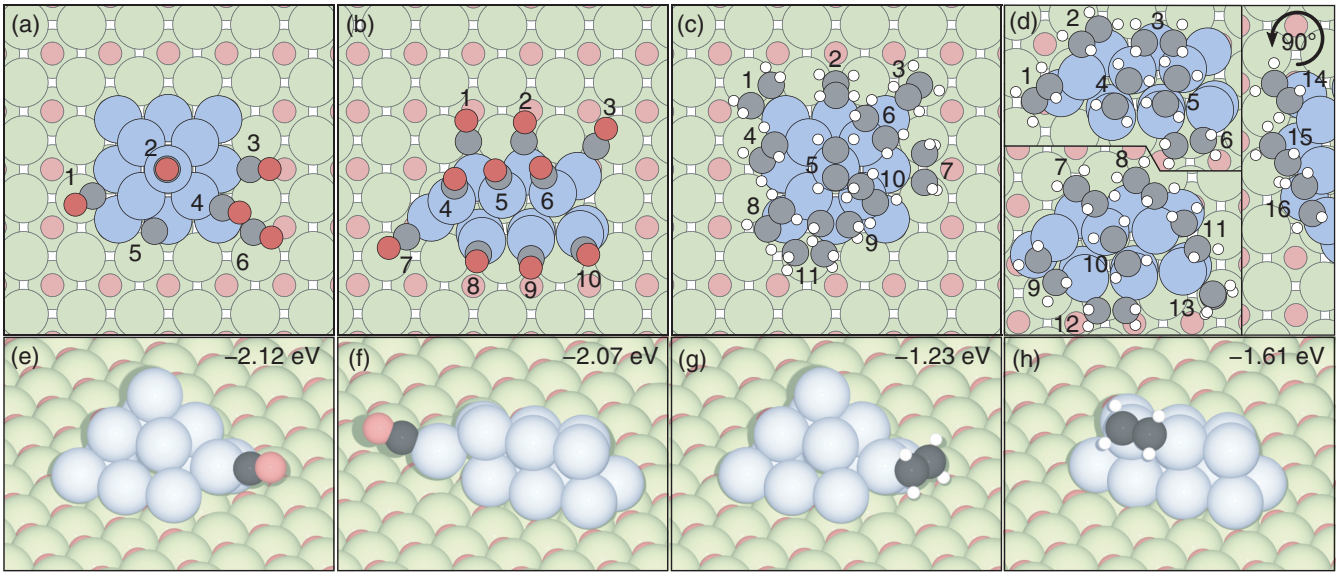

FIG. 5. The CO and C_2H_4 adsorption sites, respectively, on the hollow pyramid (a) and (c) and the elongated structure (b) and (d). The configurations pictured in (a)–(d) are of the relaxed clean structure with a schematic showing the added adsorbates. The favored adsorption configurations of CO and C_2H_4 imaged on the hollow pyramid [(e) and (g), respectively] and on the elongated structure [(f) and (h), respectively].

For the hollow pyramid, the same adsorption site is preferred whether the adsorbed molecule is a CO or an ethylene molecule. A middle interface atom is pulled slightly out and upward ∼1.23 Å from its resting position in both cases while solely bonding the adsorbate. For both molecules, there is a clear "best adsorption site" (CO: 0.22 eV and C_2H_4: 0.16 eV more stable than the second most stable). For ethylene, if we ignore the most favored adsorption, it seems that π bonding to a single Pt atom and σ bonding to two Pt atoms are relatively competitive as is seen for sites 2, 3, 5, and 6 (π bonded) versus 8, 9, 10, and 11 (σ bonded) in Fig. 5(c).

Adsorption on the elongated Pt_{13} nanoparticle is a bit more complicated as the low symmetry allows for many different adsorption sites as is seen when, e.g., comparing Figs. 5(c) and 5(d). Adsorbing CO at the most favorable site drags the immediate Pt atom ∼1.97 Å away from its resting position, a significant structural change. Ethylene on the elongated structure prefers to sit on one side of the nanoparticle bridging two Pt atoms making two σ-like bonds.

As adsorption of ethylene is significantly stronger on the elongated geometry, it is interesting to compare the relative stability of the two adsorption complexes and to consider if transforming the nanoparticle shape from the hollow pyramid to elongated is possible, perhaps during adsorption. The first is straightforward: the energy difference $E_{ad}(\text{hollow} + C_2H_4) - E_{ad}(\text{elongated} + C_2H_4) = -0.14$ eV shows that the pyramid complex is still slightly more stable; the latter is significantly more complex and is discussed in the next section.

D. Pt_{13} structure transformation

In order to determine for a given Pt nanoparticle size if the catalytic properties are governed by one particle shape or an ensemble of particle shapes, the transition barriers between particles must be known. The trained NN models lends themselves to a thorough investigation of such barriers. In Fig. 6 we consider the transition of the hollow Pt_{13} nanoparticle into the elongated Pt_{13} nanoparticle. If performed at the DFT level, only few guesses can be covered concerning which Pt atoms of the initial nanoparticle map onto which Pt atoms of the final nanoparticle. A natural choice would be the mapping that results from the Hungarian method in which the 2-norm distance of the two nanoparticles is minimized. This strategy is very similar to the approach Zhai *et al.* apply for exploring transitions between isomers of α-Al_2O_3 supported Pt_7 nanoparticles [68]. Using, however, the NN potential, a brute force strategy may be adopted to screen for the best

TABLE II. Adsorption potential energies in eV for the different adsorption sites on both the hollow pyramid and the elongated structure for both CO and C_2H_4. The bold numbers indicate the lowest energy adsorption sites of the four different nanoparticle adsorbate combinations. The corresponding structures are depicted in Fig. 5(e)–5(h).

		No.															
		1	2	3	4	5	6	7	8	9	10	11	12	13	14	15	16
CO	hPy	−1.90	−1.82	**−2.12**	−1.90	−1.73	−1.75										
	elong	−1.53	−1.91	−1.76	−1.97	−1.86	−1.48	**−2.07**	−1.94	−1.68	−1.80						
C_2H_4	hPy	−0.90	−1.05	−1.02	−0.88	−1.04	−1.07	**−1.23**	−0.99	−0.98	−1.02	−1.04					
	elong	−1.41	−1.28	−1.31	−0.55	−0.37	−1.15	−0.98	−1.05	−1.45	−0.33	−1.07	**−1.61**	−1.24	−1.23	−0.91	−1.14

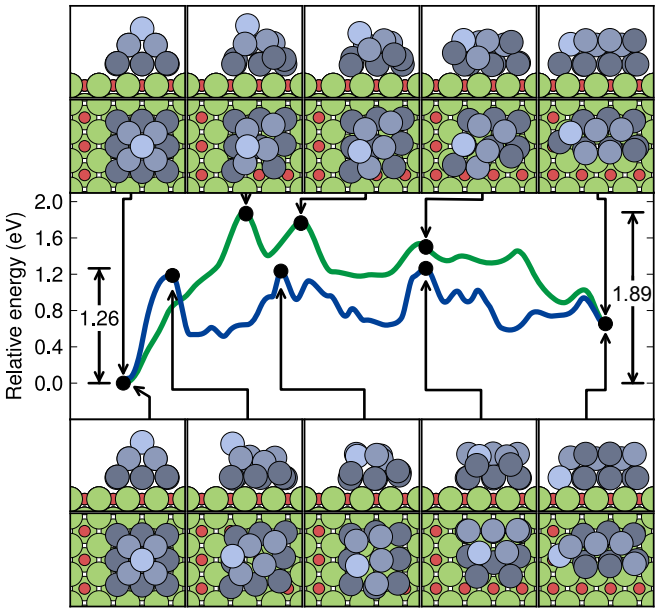

FIG. 6. The first axis shows the reaction coordinate for the transformation of the hollow pyramid to the elongated structure. The lowest-energy path is plotted in blue, while the pathway resulting from minimizing the 2-norm mapping is plotted as a reference in green. The top and bottom panels shows images of side and top views of the initial state, transition states, and final state of the two pathways. The Pt atoms are colored according to their relative height in the pyramid configuration: the lighter the blue, the higher the atoms are.

possible mapping. This is done adapting a parallel version of a machine-learning accelerated saddle-point search [51], but starting from the already trained Amp model. Collecting new training data (pathway points at the DFT level) and retraining is performed in parallel over all investigated paths using one common Amp model. Specifically, we have investigated the pathways for 600 different mappings resulting from freezing indices of five atoms, manually mapping three atoms in five different ways, and combining the remaining five Pt atoms in every conceivable way (see Supplemental Material [66], Fig. S6, for the different mappings). The rationale for fixing said indices is the like positions while the rationale for the manually shuffling of the three atoms is the desire to keep the number of pathway searches in the hundreds while still exploring any reasonable mapping.

The 600 NN-based searches were done using the AUTONEB [69] method adopting the IDPP [70] method for the initial guesses. The results showed several low-energy barrier pathways, six of which had estimated barriers less than 0.15 eV from the lowest-energy barrier. For reference, the Hungarian pathway emerged as the 71st lowest with a barrier 0.29 eV higher than the lowest. These seven pathways (including the Hungarian) were subsequently fully modeled at the DFT level and converged with very few iterations compared to what would have been required in the absence of the NN-based pathways. The mapping of the Hungarian method resulted in a barrier of 1.89 eV, while the best pathway of the six found with the systematic mapping showed a lower barrier of 1.26 eV. The corresponding energy profiles are depicted in Fig. 6 and movies of the two transitions are available in the

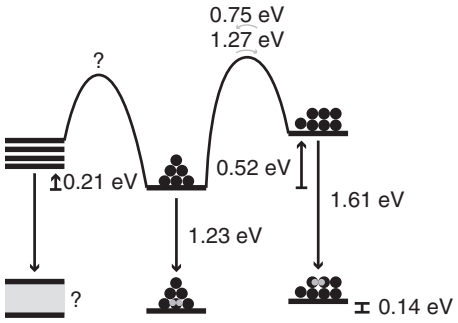

FIG. 7. Graphical representation of the two examined Pt_{13} nanoparticles with and without ethylene adsorbed. The left illustrates the possibility that one of the other stable configurations allows for an even stronger adsorption complex. The relative energy is plotted along the vertical axis and the unknown numbers are indicated with "?".

Supplemental Material [66]. The different barrier heights are crucial when preparing Pt_{13} particles for a catalytic experiment. If, at deposition of the Pt particles, elongated structures are formed they are easily converted into hollow pyramids as the barrier is "only" 0.75 eV which is manageable even at room temperature. This prediction would have been missed by only asserting the Hungarian mapping as it results in a 1.37-eV barrier which is not surpassable at room temperature. We note, however, that both the Hungarian and best systematic barrier estimates conform with the idea that as soon as hollow pyramids are formed they will be "trapped" in this state (at room temperature) as the barrier is simply too high to surmount, whether it is 1.26 or 1.89 eV does not matter.

The total stability of the most favorable elongated and pyramid ethylene complexes are almost equal but the barrier for transforming the nanoparticle from the hollow to the elongated is not expected to be dramatically reduced by adsorbing, e.g., ethylene; the exact effects though are at the moment unknown. Hence, not changing the fact that newly created particles will quickly convert to and be "trapped" as hollow pyramids even at elevated room temperature. A visual overview of the stability of the two nanoparticles (with and without adsorbed ethylene) is presented in Fig. 7. The very different adsorption configuration especially for ethylene (σ versus π bonded) and the energy difference between the two different configurations will very likely heavily influence the credibility of potential theoretical predictions of the catalytic reactivity of the real nanoparticles in practice, rendering them useless. In principle, there could be another combination of particle configuration and adsorption site that is even more stable as illustrated in the left part of Fig. 7. For the full picture situations involving different adsorbate chemical potential should also be considered. This would, however, require a detailed study and subsequent analysis and is outside the scope of this study.

Without exploring every stable nanoparticle conformation transformation barrier, we can get a feeling for how diverse the most stable conformations are and formulate qualified expectations on the distribution of experimentally found particles. This is achieved with the presumption that look-alike conformations are associated with a smaller transformation barrier and by grouping the conformations into clusters. All the unique Pt_{13}

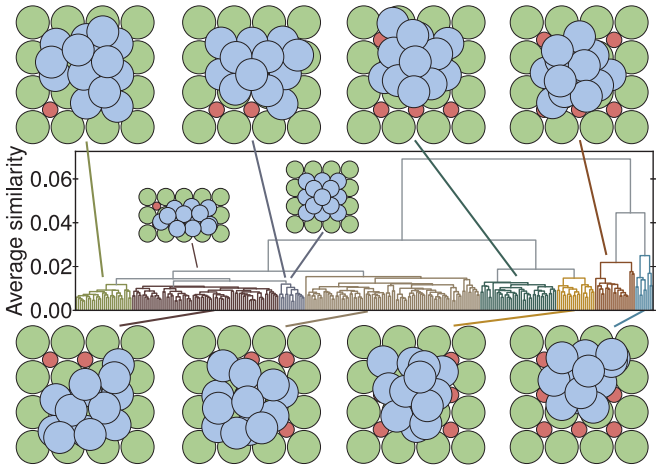

FIG. 8. A dendrogram including the eight clusters found by clustering the unique Pt_{13} structures (and the top MgO layer) following an agglomerative clustering algorithm with an average linkage and an inconsistent coefficient of 3.4 for separating clusters using the Bag of Bonds [71] fingerprint function following Ref. [60]. The hollow pyramid belongs to the purple cluster while the elongated structure belongs to the dark red cluster. For each cluster, the structure closest to the centroid has been plotted representing the geometry of the given cluster.

structures are clustered into eight clusters shown in Fig. 8 by measuring their relative similarity. For each cluster, the member closest to the centroid is visualized, as well as the cluster assignment of the hollow pyramid and the elongated structure. The five most stable structures are members of the first four clusters (from the left) with the hollow pyramid as the only member of the purple cluster. This indicates that it has no immediate very stable "relatives" suggesting, without performing the full search of every possible adsorption, mapping, and transformation, that experimentally prepared particles of 13 Pt atoms are expected to be found in this exact configuration at moderate temperatures.

IV. CONCLUSION

In summary, a neural-network-enhanced EA is outlined and applied to MgO supported Pt nanoparticles. The method proves highly CPU efficient and enables the identification of different particle shapes. This is, for instance, seen for the very stable Pt_{13} hollow pyramid. Our results highlight the need for efficient unbiased optimization methods, and the neural-network-enhanced EA described opens up for the study of, e.g., kinetic transitions between different particle shapes with the use of the on-the-fly trained neural networks. These transitions of rather diverse structures represent no easy task as is shown by investigating two Pt_{13} conformers and the "brute force" mapping allowed by our trained neural network brings the estimated barrier down by 0.62 eV compared to a mapping suggested by the Hungarian method. We show that indeed "every atom" counts and it is of utmost importance that we know every atomic position before statements on catalytic activity are made as, e.g., shown for the adsorption geometry and energy of CO and ethylene probe molecules on a Pt_{13} nanoparticle.

ACKNOWLEDGMENTS

Grants from VILLUM FONDEN (Investigator grant, Project No. 16562), Danish Council of Independent Research Natural Science (Grant No. 0602-02566B) have supported this research.

[1] D. J. Wales and J. P. K. Doye, J. Phys. Chem. A **101**, 5111 (1997).
[2] R. L. Johnston, Dalton Trans. **0**, 4193 (2003).
[3] S. Curtarolo, G. L. W. Hart, M. B. Nardelli, N. Mingo, S. Sanvito, and O. Levy, Nat. Mater. **12**, 191 (2013).
[4] J. E. Saal, S. Kirklin, M. Aykol, B. Meredig, and C. Wolverton, JOM **65**, 1501 (2013).
[5] B. R. Goldsmith, M. Boley, J. Vreeken, M. Scheffler, and L. M. Ghiringhelli, New J. Phys. **19**, 013031 (2017).
[6] J. Balluff, K. Diekmann, G. Reiss, and M. Meinert, Phys. Rev. Mater. **1**, 075502 (2017).
[7] F. A. Faber, A. Lindmaa, O. A. von Lilienfeld, and R. Armiento, Phys. Rev. Lett. **117**, 135502 (2016).
[8] M. Boudart, Adv. Cat. **20**, 153 (1969).
[9] M. Che and C. O. Bennett, Adv. Cat. **36**, 55 (1989).
[10] F. Besenbacher, I. Chorkendorff, B. S. Clausen, B. Hammer, A. M. Molenbroek, J. K. Nørskov, and I. Stensgaard, Science **279**, 1913 (1998).
[11] F. Studt, I. Sharafutdinov, F. Abild-Pedersen, C. F. Elkjær, J. S. Hummelshøj, S. Dahl, I. Chorkendorff, and J. K. Nørskov, Nat. Chem. **6**, 320 (2014).
[12] U. Heiz, A. Sanchez, S. Abbet, and W.-D. Schneider, J. Am. Chem. Soc. **121**, 3214 (1999).
[13] P. L. Hansen, J. B. Wagner, S. Helveg, J. R. Rostrup-Nielsen, B. S. Clausen, and H. Topsøe, Science **295**, 2053 (2002).
[14] Z.-P. Liu, S. J. Jenkins, and D. A. King, Phys. Rev. Lett. **94**, 196102 (2005).
[15] A. S. K. Hashmi and G. J. Hutchings, Angew. Chem. Int. Ed. **45**, 7896 (2006).
[16] T. Uchiyama, H. Yoshida, Y. Kuwauchi, S. Ichikawa, S. Shimada, M. Haruta, and S. Takeda, Angew. Chem. Int. Ed. **50**, 10157 (2011).
[17] J. K. Nørskov, T. Bligaard, J. Rossmeisl, and C. H. Christensen, Nat. Chem. **1**, 37 (2009).
[18] Y. Watanabe, Sci. Technol. Adv. Mater. **15**, 063501 (2014).
[19] A. Fernando, K. L. D. Weerawardene, N. V. Karimova, and C. M. Aikens, Chem. Rev. **115**, 6112 (2015).
[20] N. Artrith, B. Hiller, and J. Behler, Phys. Status Solidi B **250**, 1191 (2013).
[21] M. Hellström, D. Spångberg, K. Hermansson, and P. Broqvist, J. Phys. Chem. C **118**, 6480 (2014).
[22] N. Artrith and A. M. Kolpak, Comput. Mater. Sci. **110**, 20 (2015).
[23] S. Schauermann and H.-J. Freund, Acc. Chemi. Res. **48**, 2775 (2015).
[24] A. R. Oganov and C. W. Glass, J. Chem. Phys. **124**, 244704 (2006).
[25] L. B. Vilhelmsen and B. Hammer, J. Chem. Phys. **141**, 044711 (2014).
[26] D. J. Wales and H. A. Scheraga, Science **285**, 1368 (1999).

[27] S. Goedecker, J. Chem. Phys. **120**, 9911 (2004).
[28] S. Hajinazar, J. Shao, and A. N. Kolmogorov, Phys. Rev. B **95**, 014114 (2017).
[29] M. Rupp, A. Tkatchenko, K.-R. Müller, and O. A. von Lilienfeld, Phys. Rev. Lett. **108**, 058301 (2012).
[30] E. D. Cubuk, S. S. Schoenholz, J. M. Rieser, B. D. Malone, J. Rottler, D. J. Durian, E. Kaxiras, and A. J. Liu, Phys. Rev. Lett. **114**, 108001 (2015).
[31] A. P. Bartók, M. C. Payne, R. Kondor, and G. Csányi, Phys. Rev. Lett. **104**, 136403 (2010).
[32] A. P. Bartók and G. Csányi, Int. J. Quantum Chem. **115**, 1051 (2015).
[33] V. L. Deringer and G. Csányi, Phys. Rev. B **95**, 094203 (2017).
[34] S. Chmiela, A. Tkatchenko, H. E. Sauceda, I. Poltavsky, K. T. Schütt, and K.-R. Müller, Sci. Adv. **3**, e1603015 (2017).
[35] T. L. Jacobsen, M. S. Jørgensen, and B. Hammer, Phys. Rev. Lett. **120**, 026102 (2018).
[36] V. L. Deringer, C. J. Pickard, and G. Csányi, Phys. Rev. Lett. **120**, 156001 (2018).
[37] S. Lorenz, A. Groß, and M. Scheffler, Chem. Phys. Lett. **395**, 210 (2004).
[38] J. Behler and M. Parrinello, Phys. Rev. Lett. **98**, 146401 (2007).
[39] J. Behler, Phys. Chem. Chem. Phys. **13**, 17930 (2011).
[40] P. E. Dolgirev, I. A. Kruglov, and A. R. Oganov, AIP Advances **6**, 085318 (2016).
[41] H. Zhai and A. N. Alexandrova, J. Chem. Theory Comput. **12**, 6213 (2016).
[42] A. Khorshidi and A. A. Peterson, Comput. Phys. Commun. **207**, 310 (2016).
[43] Z. Li, J. R. Kermode, and A. De Vita, Phys. Rev. Lett. **114**, 096405 (2015).
[44] T. K. Patra, V. Meenakshisundaram, J.-H. Hung, and D. S. Simmons, ACS Comb. Sci. **19**, 96 (2017).
[45] R. Ouyang, Y. Xie, and D.-E. Jiang, Nanoscale **7**, 14817 (2015).
[46] Q. Tong, L. Xue, J. Lv, Y. Wang, M. Yanchao, and Y. Ma, Faraday Discuss (2018), doi:10.1039/C8FD00055G.
[47] S. Q. Wu, M. Ji, C. Z. Wang, M. C. Nguyen, X. Zhao, K. Umemoto, R. M. Wentzcovitch, and K. M. Ho, J. Phys.: Condens. Matter **26**, 035402 (2014).
[48] M. Van den Bossche, H. Grönbeck, and B. Hammer, J. Chem. Theory Comput. **14**, 2797 (2018).
[49] K. W. Jacobsen, P. Stoltze, and J. K. Nørskov, Surf. Sci. **366**, 394 (1996).
[50] A. Larsen, J. J. Mortensen, J. Blomqvist, I. E. Castelli, R. Christensen, M. Dułak, J. Friis, M. N. Groves, B. Hammer, C. Hargus *et al.*, J. Phys.: Condens. Matter **29**, 273002 (2017).
[51] A. A. Peterson, J. Chem. Phys. **145**, 074106 (2016).
[52] J. S. Smith, O. Isayev, and A. E. Roitberg, Chem. Sci. **8**, 3192 (2017).
[53] J. R. Boes and J. R. Kitchin, J. Phys. Chem. C **121**, 3479 (2017).
[54] J. R. Boes and J. R. Kitchin, Mol. Simul. **43**, 346 (2017).
[55] Z. W. Ulissi, M. T. Tang, J. Xiao, X. Liu, D. A. Torelli, M. Karamad, K. Cummins, C. Hahn, N. S. Lewis, T. F. Jaramillo, K. Chan, and J. K. Nørskov, ACS Catalysis **7**, 6600 (2017).
[56] J. Enkovaara, C. Rostgaard, J. J. Mortensen, J. Chen, M. Dułak, L. Ferrighi, J. Gavnholt, C. Glinsvad, V. Haikola, H. A. Hansen *et al.*, J. Phys.: Condens. Matter **22**, 253202 (2010).
[57] A. S. Crampton, M. D. Rötzer, C. J. Ridge, B. Yoon, F. F. Schweinberger, U. Landman, and U. Heiz, Surf. Sci. **652**, 7 (2016).
[58] A. S. Crampton, M. D. Rötzer, C. J. Ridge, F. F. Schweinberger, U. Heiz, B. Yoon, and U. Landman, Nat. Commun. **7**, 10389 (2016).
[59] J. P. Perdew, K. Burke, and M. Ernzerhof, Phys. Rev. Lett. **77**, 3865 (1996).
[60] M. S. Jørgensen, M. N. Groves, and B. Hammer, J. Chem. Theory Comput. **13**, 1486 (2017).
[61] S. E. Deutsch, J. T. Miller, K. Tomishige, Y. Iwasawa, W. A. Weber, and B. C. Gates, J. Phys. Chem. **100**, 13408 (1996).
[62] J. Goniakowski, A. Jelea, C. Mottet, G. Barcaro, A. Fortunelli, Z. Kuntová, F. Nita, A. C. Levi, G. Rossi, and R. Ferrando, J. Chem. Phys. **130**, 174703 (2009).
[63] J. Goniakowski and C. Mottet, Phys. Rev. B **81**, 155443 (2010).
[64] E. Florez, F. Mondragon, and F. Illas, Surf. Sci. **606**, 1010 (2012).
[65] K. Rossi, T. Ellaby, L. O. Paz-Borbón, I. Atanasov, L. Pavan, and F. Baletto, J. Phys.: Condens. Matter **29**, 145402 (2017).
[66] See Supplemental Material at http://link.aps.org/supplemental/10.1103/PhysRevB.97.195424 for an extensive view of the located Pt nanoparticles, the mapping procedure for the configuration transformation, and movies of the compared transformation paths.
[67] R. Ferrando, G. Barcaro, and A. Fortunelli, Phys. Rev. B **83**, 045418 (2011).
[68] H. Zhai and A. N. Alexandrova, J. Phys. Chem. Lett. **9**, 1696 (2018).
[69] E. L. Kolsbjerg, M. N. Groves, and B. Hammer, J. Chem. Phys. **145**, 094107 (2016).
[70] S. Smidstrup, A. Pedersen, K. Stokbro, and H. Jónsson, J. Chem. Phys. **140**, 214106 (2014).
[71] K. Hansen, F. Biegler, R. Ramakrishnan, W. Pronobis, O. A. von Lilienfeld, K.-R. Müller, and A. Tkatchenko, J. Phys. Chem. Lett. **6**, 2326 (2015).